SCIENTIFIC REPORTS
nature research

OPEN

Hierarchical multi-shell hollow micro–meso–macroporous silica for Cr(VI) adsorption

Roozbeh Soltani[1], Azam Marjani[1], Reza Soltani[2] & Saeed Shirazian[3,4]✉

The development of easier, cheaper, and more effective synthetic strategies for hierarchical multimodal porous materials and multi-shell hollow spheres remains a challenging topic to utilize them as adsorbents in environmental applications. Here, the hierarchical architecture of multi-shell hollow micro–meso–macroporous silica with pollen-like morphology (MS-HMS-PL) has been successfully synthesized *via* a facile soft-templating approach and characterized for the first time. MS-HMS-PL sub-microspheres showed a trimodal hierarchical pore architecture with a high surface area of 414.5 $m^2 g^{-1}$, surpassing most of the previously reported multishelled hollow nanomaterials. Due to its facile preparation route and good physicochemical properties, MS-HMS-PL could be a potential candidate material in water purification, catalysis, and drug delivery. To investigate the applicability of MS-HMS-PL as an adsorbent, its adsorption performance for Cr(VI) in water was evaluated. Important adsorption factors affecting the adsorption capacity of adsorbent were systematically studied and Kinetics, isotherms, and thermodynamics parameters were computed *via* the non-linear fitting technique. The maximum capacity of adsorption computed from the Langmuir isotherm equation for Cr(VI) on MS-HMS-PL was 257.67 mg g^{-1} at 293 K and optimum conditions (pH 4.0, adsorbent dosage 5.0 mg, and contact time 90 min).

During the past decades, tremendous progress has been made in the design, synthesis, and application of hierarchical multi-shell hollow micro-meso-macroporous (MS-HM) architectures. These materials possess marvelous features, including low density, large surface area, the void spacing between the shells, high loading capacity, and good desorption performance, which endow them with widespread potential applications in water treatment, drug delivery, supercapacitors, fuel cells, nano-reactors, catalysis, dye-sensitized solar cells, and sensors[1–4]. These materials with triple or more hollow vesicles or lamellar shells are expected to yield better performances than their single- or double-shell nanoporous counterparts, although their synthesis routes are not straightforward similar to those with single- or double-shell owing to the increased complexity of the structure[4].

The literature reveals that the nanoporous silica materials have attracted a great deal of attention compared with other porous materials due to their easily accessible starting materials, biodegradability, functionalizability, environmentally friendly nature, and high chemical and mechanical stability[5–9]. Hierarchically structured MS-HM silica (MS-HMS) materials have the advantages of both nanoporous silica and multi-shell hollow structures. Synthesis of MS-HMSs—mainly constituted of various sequences of interconnected pores of different sizes ranging from micro-(<2 nm), meso-(2–50 nm), to macropores (>50 nm)—offers an intelligent strategy to promote the adsorption properties, catalysis performance, and drug loading/releasing ability through minimizing diffusion barriers[6,10,11]. However, until now, there are relatively few studies that have reported the synthesis of MS-HMS materials. Zhao and co-workers (2010) reported a synthesis route for the preparation of carbon-silica composite with a multilayer vesicular structure using the aqueous emulsion-hydrothermal method from multi-constituent co-assembly of preformed resols, trimethyl benzene, Pluronic F127, and silicate oligomers in an acidic solution[12]. Yeh and co-workers (2011) reported the fabrication of triple-shelled silica nanospheres (with a surface area of 329.2 $m^2 g^{-1}$) through a hard-templating technique using polystyrene nanoparticles as a template[13]. A sacrificial template method, proposed by Ma and co-workers (2017), could also be used for the preparation of

[1]Department of Chemistry, Arak Branch, Islamic Azad University, Arak, Iran. [2]Department of Chemistry, Lorestan University, Khoramabad, Iran. [3]Department for Management of Science and Technology Development, Ton Duc Thang University, Ho Chi Minh City, Vietnam. [4]Faculty of Applied Sciences, Ton Duc Thang University, Ho Chi Minh City, Vietnam. ✉e-mail: saeed.shirazian@tdtu.edu.vn

the triple-shelled hollow silica microspheres possessing a hierarchically porous structure with a surface area of 35 $m^2 g^{-1}$ [14].

Although these above-mentioned preparation methods report a multi-shell hollow structure, a tedious and complicated multi-step synthesis procedure or a low surface area silica product limited the availability or usability of the aforementioned templating methods. Another synthesis protocol for MS-HMS materials was introduced in 2019 by Soltani et al. where shell-in-shell functionalized silica hollow microspheres with mesoporous structure may be synthesized *via* a soft-templating method[15]. Although this method uses a simple and one-step synthesis procedure, however, this material has a low surface area of 29 $m^2 g^{-1}$. All the aforementioned MS-HMS materials have mesoporous layers or shells on their structures, and mesopores are the major constituent of these structures.

In this work, we report for the first time the synthesis of hierarchically architectured MS-HMS with pollen-like morphology (MS-HMS-PL) and uniform lamellar structure through a facile and one-step conventional soft-templating assisted hydrothermal method. Interestingly, MS-HMS displays a trimodal micro-meso-macrostructure. Hierarchically MS-HMS sub-microspheres with a majority of micropores in their lamellar shells and a high surface area of up to 414.5 $m^2 g^{-1}$ have not been synthesized until now. To investigate the adsorption efficiency and the applicability of the MS-HMS-PL for removal of toxic and highly mobile hexavalent chromium (Cr(VI)), its adsorption performance for Cr(VI) was evaluated. The adsorption technique, especially for removing toxic metals from water, has attracted a great deal of attention in recent years owing to its high efficiency, ease of operation, reusability, insensitivity to hazardous pollutants, use of a wide variety of adsorbents with designable structures, and availability of different adsorbents with relatively low-cost[5,6,15,16]. Among the potential toxic metals, Cr(VI) was chosen because it is generated mainly due to human anthropological activities (*e.g.*, cement, leather tanning, electroplating, and textile industries) and is present in industrial wastes and possesses strong toxicity, mutagenicity, and carcinogenicity[16–18]. Important adsorption factors affecting the adsorption performance of the adsorbent toward Cr(VI) were systematically monitored and isotherms, kinetics, and thermodynamics parameters were estimated *via* the non-linear fitting method.

Results and Discussion

Synthesis of MS-HMS-PL. MS-HMS-PL was synthesized by a simple soft-templating hydrothermal method. The formation of multi-shell MS-HMS-PL implies the presence of multi-lamellar CTAB hollow spheres (Fig. 1, the formation of CTAB lamellar layers). The self-assembly of amphiphilic CTAB molecules in basic aqueous ammonia solution and the presence of 1-pentanol as co-surfactant leads to the formation of micelles and closed multi-layer hollow aggregates. The role of CTAB molecules is a structure-directing agent where *in-situ* polymerization of TEOS (in the basic condition) on the surface of preformed lamellar layers constructed by CTAB molecules leads to a hybrid organic-inorganic wall. After hydrothermal condition and complete polymerization of TEOS between CTAB layers (as depicted in Fig. 1), subsequent calcination was applied to remove the structure-directing agent and produce a stable MS-HMS-PL. In summary, we have developed a simple synthesis approach to the preparation of novel hierarchically architectured multi-shell hollow micro-meso-macroporous silica with pollen-like morphology. This material may have the potential for many uses in the fields of adsorption, analytical extraction, catalysis, carries, and drug release with prolonged-release time.

Structure characterization of MS-HMS-PL. *XRD analysis.* To understand the crystalline structure of the MS-HMS-PL, L-XRD pattern of the sample is investigated. The L-XRD pattern of the MS-HMS-PL is shown in Fig. 2a. This silica material revealed only a broad diffraction peak at 2 θ 1° to 4°, implying the low ordering of silica framework in MS-HMS-PL.

FT-IR measurement. The FT-IR spectrum of MS-HMS-PL was recorded and is shown in Fig. S1. All characteristic absorption bands related to the nanoporous silica framework were observed for MS-HMS-PL (at 465 cm^{-1}: bending mode of Si–O–Si; at 802 cm^{-1}: symmetric mode of Si–O–Si vibration; at 964 cm^{-1}: stretching mode of Si–OH; at 1088 and 1235 cm^{-1}: asymmetric Si–O–Si vibration; 1626 cm^{-1}: bending mode of surface adsorbed H_2O; 3247 cm^{-1}: O–H stretching modes of silanol groups) which were in close agreement with previously reported silica-based materials with nanoporous structures[9,19,20]. On a literature basis, a broad intense band between 3100-3750 cm^{-1} is attributed to the different silanol species (3650–3200 cm^{-1}: O–H stretching modes of strongly hydrogen-bonded sialons in the silica framework; above 3650 cm^{-1}: O–H stretching modes of isolated or free sialons)[21].

Nitrogen adsorption-desorption isotherms. Nitrogen adsorption-desorption analysis was conducted with the aim of further investigating the structural feature of MS-HMS-PL. According to the IUPAC classification, MS-HMS-PL showed a combination of Type I(b) and IV isotherms with a Type H3 hysteresis loop at a relative pressure above 0.5 (Fig. 2b), suggesting the adsorption of N_2 molecules in the hollow voids (macropores, Fig. 1)[22–24]. Type I(b) isotherms are representative of materials having pore size distributions in the range of wider micropores (<2 nm) and possibly narrow mesopores (<∼2.5 nm). Type IV isotherms are given by mesoporous materials. The BET surface area and total pore volume measured to be 414.5 $m^2 g^{-1}$ and 0.39 $cm^3 g^{-1}$ for MS-HMS-PL (Table S1). Using the Barrett–Joyner– Halenda (BJH) method, the average pore sized of MS-HMS-PL is estimated to be 1.22 nm. Accordingly, the macropores are related to the hollow space in the middle of the MS-HMS-PL sub-microspheres, and the micro-/mesopores are located within the multi-lamellar layers of MS-HMS-PL. The mesopores with the pore size in the range of 2-4 nm are also observed in the BJH pore size distribution curve. All of the above results clearly indicate that MS-HMS-PL sub-microspheres possess a trimodal hierarchical pore architecture including micropores (the major constituent of lamellar shells), mesopores (the minor constituent of lamellar shells), and macropores (in the middle of sub-microspheres). This trimodal hierarchical pore structure is given in a schematic representation in Fig. 1.

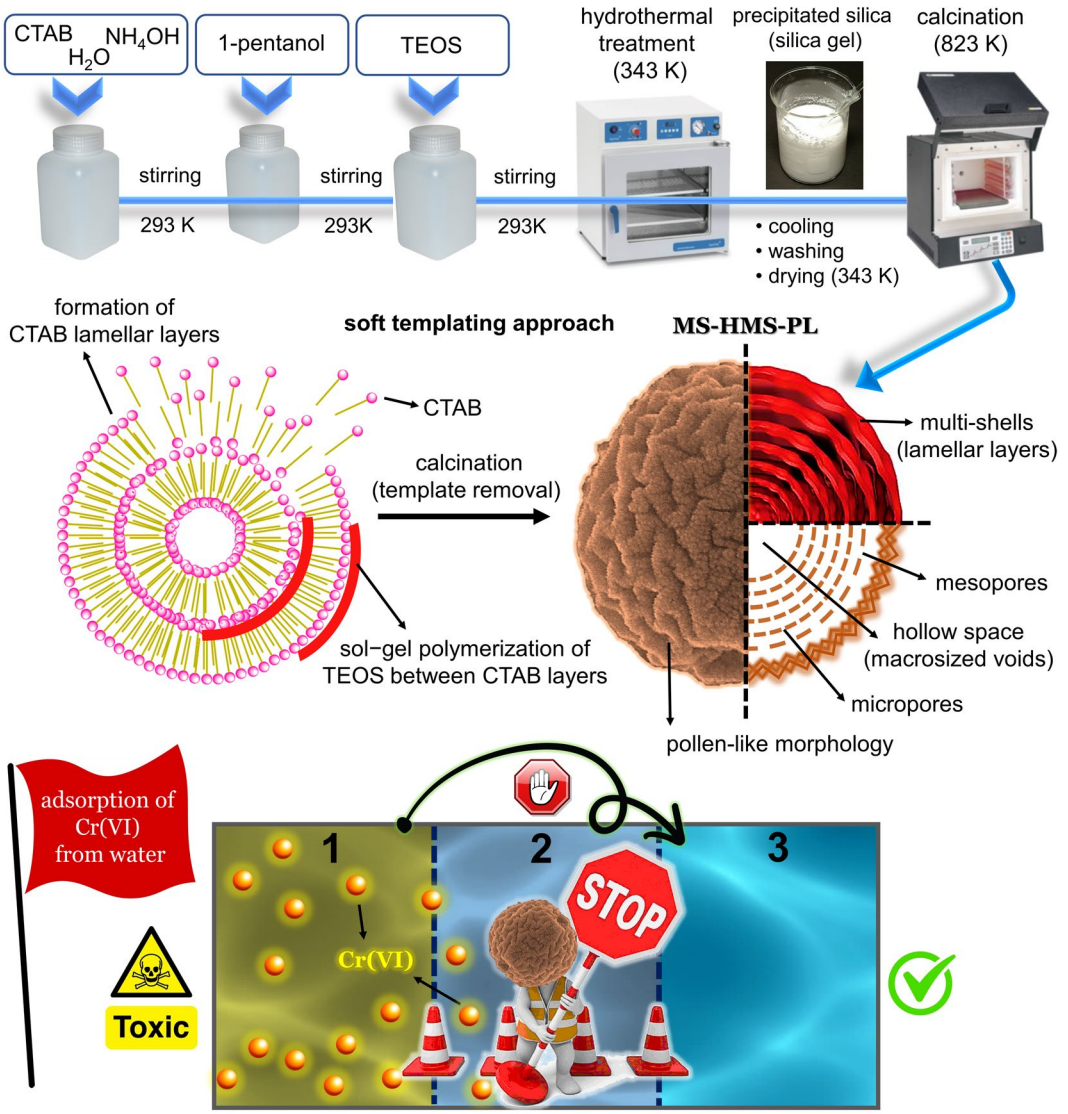

Figure 1. Schematic illustration of the synthesis procedure of hierarchically architectured MS-HMS-PL *via* soft-templating method and its application for Cr(VI) removal from the aqueous solution.

Some typical hollow single, double, and multi-shell nanomaterials reported in the last decade are summarized in Table 1, and their properties including their composition, synthesis method, surface area, and pore size characteristics are also given. The BET surface area of MS-HMS-PL was 414.5 $m^2 g^{-1}$, surpassing most of the previously reported hollow nanomaterials. Furthermore, as shown in Table 1, unlike the reported materials in which mesopores are the major constituent of structure, the major constituent of lamellar shells in MS-HMS-PL sub-microspheres is micropores. With its trimodal hierarchical architecture and relatively high surface area, MS-HMS-PL could be a potential candidate for adsorption, extraction, catalysis, and drug delivery applications.

FE-SEM and TEM micrographs. The FE-SEM micrographs of the MS-HMS-PL as shown in Fig. 2c–e revealed that this material is highly dispersed and possesses uniform pollen-like morphology. The magnified FE-SEM image (Fig. 2e) gave further information about the surface of the MS-HMS-PL with a wrinkled surface which can increase the accessible external surface area compared to the flat smooth surface. The TEM image of MS-HMS-PL (Fig. 2g) clearly shows that the particles possess a hollow spherical structure with a multi-lamellar shell. The schematic structure representation of MH-HMS-PL is shown in Fig. 2f.

Application of MS-HMS-PL as an adsorbent in the removal of Cr(VI) from aqueous solution. The important factors including pH, the dosage of adsorbent, contact time, initial Cr(VI) concentrations, and temperature, affecting the adsorption performance of MS-HMS-PL were systematically monitored. The adsorption kinetics, isotherms, and thermodynamics of Cr(VI) on MS-HMS-PL in aqueous solutions were investigated by conducting a series of kinetics, isotherms, and thermodynamic studies. The experimental adsorption data were fitted to the various kinetics and isotherms by the nonlinear method. According to the literature, the nonlinear method is a better way to obtain the kinetics and isotherm parameters because the linearization

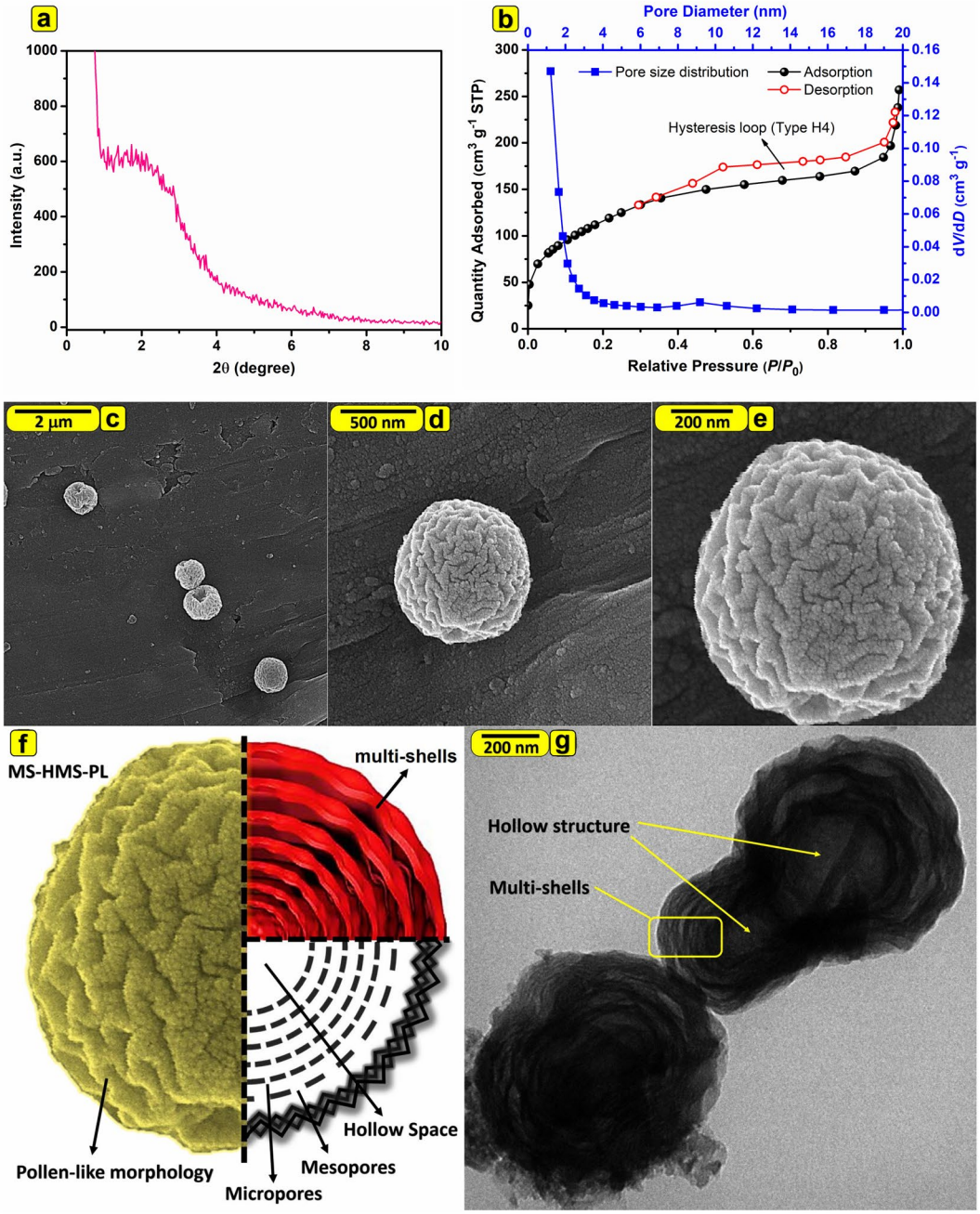

Figure 2. (**a**) L-XRD pattern of MS-HMS-PL. (**b**) N_2 adsorption-desorption isotherms of MS-HMS-PL at 77 K and the BJH pore size distribution (pore diameter *vs* d*V*/d*P*) curve from the adsorption isotherm. (**c**–**e**) The FE-SEM, (**f**) the schematic structure representation, and (**g**) TEM micrograph of MS-HMS-PL.

of nonlinear kinetic and isotherm expressions usually distort the fit by changing the error distributions[5–7,25–27]. The nonlinear forms of different kinetic (Eqs. 5–8) and isotherm models (Eqs. 9–11), as well as thermodynamic equations (Eqs. 12–14), and their parameters are tabulated in Table 2.

pH and adsorbent dosage. The influence of pH on the removal percentage of Cr(VI) at three different dosages of adsorbent was tested and is shown in Fig. S2. From Fig. S2, the maximum removal percentage achieved at pH 4.0 and exceeded ~93% at all three dosages of the adsorbent. At this solution pH, the removal percentages of ~93%, ~97%, and ~99% were obtained for adsorbent dosages of 2.0, 5.0, and 8.0 mg, respectively. Accordingly, pH 4.0 and adsorbent dosage of 5.0 mg were used for next adsorption studies as optimum conditions. The removal percentage decreased continuously with the increase of pH values and ~72% Cr(VI) was removed at pH 8.0 and 5.0 mg adsorbent dosage. Decreasing the solution pH below 4.0 leads to a decrease in the removal percentage and the adsorbent removed ~67% Cr(VI) at pH 2.0 and 5.0 mg adsorbent dosage. According to the literature, silica-based adsorbents are deprotonated above pH 4.5-5.0[10,28,29] and this may be the reason for decreasing the

year	Material	Composition	method	S_{BET}(m^2g^{-1})	*D* (nm)	Ref.
2010	MLV-CS	Carbon-SiO_2	HT	329	5.3	[12]
2010	MLV-S-Cal	SiO_2	HT	598	14.4	[12]
2010	MLV-S-MWD	SiO_2	HT	530	22.6	[12]
2010	MMSHNs-4	SiO_2	ST	414	4.1	[23]
2010	MMSHNs-5	SiO_2	ST	385	3.9	[23]
2010	MMSHNs-6	SiO_2	ST	453	2.6	[23]
2011	single-shelled silica	SiO_2	HT	155.2	<8	[13]
2011	double-shelled silica	SiO_2	HT	243.9	~11	[13]
2011	triple-shelled silica	SiO_2	HT	329.2	~11	[13]
2013	triple shells SnO_2 HMSs	SnO_2	HT	32.84	not reported	[35]
2013	quadruple shells SnO_2 HMSs	SnO_2	HT	36.27	not reported	[35]
2013	quintuple shells SnO_2 HMSs	SnO_2	HT	38.74	not reported	[35]
2014	double-shelled Mn_2O_3	Mn_2O_3	HT	27.71	not reported	[33]
2014	triple-shelled Mn_2O_3	Mn_2O_3	HT	36.55	not reported	[33]
2014	quadruple-shelled Mn_2O_3	Mn_2O_3	HT	30.22	not reported	[33]
2014	SS-TiO_2-HNPs	TiO_2	HT	63.6	not reported	[36]
2014	DS-TiO_2-HNPs	TiO_2	HT	128.4	not reported	[36]
2014	MS-TiO_2-HNPs	TiO_2	HT	171.3	4.1	[36]
2014	Co_3O_4 yolk–shell powders	Co_3O_4	HT	1.5-6.2	5-60	[37]
2015	Fe_3O_4@MnO_2 BBHs	Fe_3O_4- MnO_2	HT	247.9	3.7	[1]
2019	multi-shelled TAS-HMSs	SiO_2	ST	29	<20	[15]
2020	MS-HMS-PL	SiO_2	ST	414.5	1.22	This work

Table 1. Selection of the textural properties of some hollow single, double, and multi-shell nanomaterials in the last decade (HT, ST, S_{BET}, and *D* are the hard-templating method, soft-templating method, BET surface area, and pore size, respectively)[a]. [a]MLV-CS: multilayer vesicle carbon–silica composite; MLV-S-Cal: MLV calcined silica; MLV-S-MWD: the silica vesicles from the microwave digestion method; MMSHNs: multi-shelled mesoporous silica hollow nanospheres; SS-TiO_2-HNPs: single-shell TiO_2 hollow nanoparticles; DS-TiO_2-HNPs: double-shell TiO_2-HNPs; MS-TiO_2-HNPs: multi-shell TiO_2-HNPs; TSHMs: triple-shell hollow microspheres; BBHs: ball-in-ball hollow spheres; TAS-HMSs: triamine-functionalized SiO_2 hollow microspheres; MSHSs: multi-shelled hollow spheres.

removal percentage of Cr(VI) anions at higher pH as a consequence of electrostatic repulsion between Cr(VI) oxyanions and negatively charged surface of MS-HMS-PL. Also, the lower amount of removal percentage at lower pHs may be due to the high concentration of H_3O^+ cations in acidic media where the interactions of Cr(VI) anions with H_3O^+ cations are more effective than the adsorbent surface. At acidic aqueous media lower than 6.0, the dominant species are $HCrO_4^-$ (pH 2.0-5.0) and CrO_4^{2-} (pH > 5.5).

Effect of time and initial concentration. The simultaneous influence of time and initial concentration changes on the adsorption capacity of adsorbent and removal percentage of Cr(VI) was monitored under constant conditions (Fig. 3a,b; figure caption for details). As shown in Fig. 3a, the adsorption capacity of the MS-HMS-PL increased with augmenting the initial concentration of Cr(VI) from 5 to 200 mg L^{-1}. However, the removal percentage decreased with augmenting the initial concentration of Cr(VI) as shown in Fig. 3b. The experimental adsorption capacity after reaching equilibrium ($Q_{e,exp}$/mg g^{-1}) for certain initial concentrations are given in Table 3. When the initial concentration of Cr(VI) was 5 mg L^{-1}, the adsorption capacity was 19.89 mg g^{-1} (%Removal = 99.46%). The adsorption capacity increased to 270.14 mg g^{-1} (%Removal = 33.77%) at an initial concentration of 200 mg L^{-1}.

The adsorption of Cr(VI) occurs in three consecutive steps:

(I) An initial fast step that lasts for 30 min
(II) The slower adsorption process in the range from 30 to 90 min
(III) An almost constant absorption step with very little variation in the adsorption rate where further increase in contact time does not reveal an increase in removal percentage of Cr(VI) or adsorption capacity of the adsorbent.

Consequently, 90 min was selected as optimum contact time to ascertain the equilibrium uptake of Cr(VI) to the MS-HMS-PL in the following experiments.

Kinetic and isotherm studies. In order to investigate the regulation of Cr(VI) uptake on MS-HMS-PL, four different kinetic models, *viz*., pseudo-first-order (PFO), pseudo-second-order (PSO), Elovich, and intra-particle diffusion (IPD), were used to fit the experimental data. Kinetics for the Cr(VI) adsorption onto MS-HMS-PL

Eq.	Kinetic equations		
5	PFO	$Q_t = Q_{e,\,cal.} \cdot (1 - e^{-k_1 \cdot t})$	$Q_{e,\,cal.}$: the calculated adsorption capacity at any time t (mg g^{-1}) k_1: the PFO rate constant of adsorption (min^{-1})
6	PSO	$Q_t = \frac{Q_{e,cal.}^2 \cdot k_2 \cdot t}{1 + Q_{e,cal.} \cdot k_2 \cdot t}$	k_2: the PSO rate constant of adsorption (g mg^{-1} min^{-1})$h(h = Q_{e,cal.}^2 \cdot k_2)$: the initial adsorption rate (mg g^{-1} min^{-1})
7	Elovich	$Q_t = \frac{1}{\beta} \ln\left(\alpha \cdot \beta\right) \cdot t$	α: the initial adsorption rate (mg g^{-1} min^{-1})β: kinetic parameter related to the activation energy for chemisorption and extent of surface coverage (g mg^{-1})
8	IPD	$Q_t = k_{IPD} \cdot t^{0.5} + C$	k_{IPD}: intra-particle diffusion rate constant (mg g^{-1} min$^{-0.5}$)C: intra-particle diffusion constant related to the thickness of the boundary layer (mg g^{-1})
	Isotherm equations		
9	Langmuir	$Q_e = \frac{Q_{m,cal} K_L C_e}{1 + K_L C_e}$	$Q_{m,cal.}$: the theoretical maximum adsorption capacity (mg g^{-1}) K_L: the Langmuir equilibrium constant (L mg^{-1}) R_L ($R_L = [1/(1 + K_L \cdot C_e)]$): the separation factor (−)
10	Freundlich	$Q_e = K_F C_e^{1/n}$	K_F: Freundlich constant ((mg g^{-1}) (L mg^{-1})$^{1/n}$) n: adsorption intensity (−)
11	R-P	$Q_e = \frac{K_{R-P} C_e}{1 + \alpha_{R-P} C_e^g}$	K_{R-P}: Redlich-Peterson isotherm constant (L g^{-1}) α_{R-P}: Redlich-Peterson isotherm constant (mg L^{-1})$^{-g}$ g: Redlich-Peterson isotherm binding constant ($0 < g < 1$)
	Thermodynamic equations		
12	$K_e^o = \frac{1000 \cdot K_L \cdot MW \cdot [adsorbate]^o}{\gamma}$		K_e^o: thermodynamic equilibrium constant (−) MW: the molecular weight of the adsorbate (g mol^{-1}) $[absorbate]^o$: the unitary standard concentration of the adsorbate (1 mol L^{-1}) γ: the coefficient of activity (−)
13	$\ln K_e^o = -\frac{\Delta H_{ads.}^o}{R} \cdot \frac{1}{T} + \frac{\Delta S_{ads.}^o}{T}$		R: the universal gas constant (J mol^{-1} k^{-1}) $\Delta H_{ads.}^o$: standard enthalpy changes of adsorption (kJ mol^{-1}) $\Delta S_{ads.}^o$: standard entropy changes of adsorption (J mol^{-1} K^{-1})
14	$\Delta G_{ads.}^o = \Delta H_{ads.}^o - T \cdot \Delta S_{ads.}^o$		$\Delta G_{ads.}^o$: standard Gibbs free changes of adsorption (kJ mol^{-1})

Table 2. Non-linear form of Kinetic, isotherm, and thermodynamic equations and their parameters.

were systematically studied at eight different initial concentrations (5–200 mg L^{-1}) and the results are given in Table 3. The corresponding curves in Fig. 3c are the PFO, PSO, and Elovich models after non-linear fitting at an initial concentration of 200 mg L^{-1} (figure caption for details). From Table 3, for non-linear kinetic models, the R^2 values of the PSO kinetic model were higher than those of PFO and Elovich models at all the initial Cr(VI) concentrations. For the initial concentration of 200 mg L^{-1}, Table 3, the R^2 values of the PFO, PSO, and Elovich models were respectively 0.8905, 0.9893, 0.9470, implying that PSO kinetic model gives the best fit to the data. Also, the experimental adsorption capacity at equilibrium, $Q_{e,exp} = 270.14$ mg g^{-1}, was very close to the calculated adoption capacity at equilibrium, $Q_{e,cal} = 278.55$ mg g^{-1}, obtained from the PSO model at the initial concentration of 200 mg L^{-1}. Accordingly, the adsorption process of Cr(V) by MS-HMS-PL could be well represented by the non-linear PSO kinetic model for all eight concentrations. Fitting of the nonlinear PFO, PSO, and Elovich kinetic models for eight different initial concentrations is depicted in Fig. S3.

IPD kinetic model (Eq. 8) was used so as to gain a better understanding of the mechanism involved in the Cr(VI) adsorption on the MS-HMS-PL. Figure 3d shows the three-stage-adsorption process in the plots of Q_t versus $t^{0.5}$ for the adsorption of Cr(VI) on the adsorbent, implying that more than one mechanism affected the adsorption process. Adsorption of Cr(VI) by hierarchically architectured MS-HMS-PL occurs in the three consecutive stages according to Fig. 3d:

(I) The First stage is attributed to the fast-external surface adsorption throughout the boundary layer film (external mass transfer) of liquid surrounding the outside of MS-HMS-PL
(II) The second stage is fast external or internal adsorption at a site on the MS-HMS-PL surface and the adsorption energy will directly relate to the type of interaction between Cr(VI) and MS-HMS-PL
(III) The third stage refers to the intraparticle diffusion mechanism as a rate-controlling step (gradual absorption by diffusion of the Cr(VI) anions to MS-HMS-PL site either *via* a solid surface diffusion or *via* a pore diffusion mechanism through the liquid-filled pores).

Figure S4 is the plot of Qt vs. $t^{0.5}$ at different initial Cr (VI) concentrations and corresponding IPD kinetic parameters are given in Table 3.

Parameters of adsorption isotherms for a target adsorbate are of great significance for evaluating and predicting the adsorption behavior of an adsorbent. Two two-parameter isotherm models (namely the Langmuir and Freundlich models; Table 1 Eqs. 9 and 10) and a three-parameter isotherm model (namely Redlich-Peterson model; eq. 11) were used to evaluate the equilibrium data for adsorptive removal of Cr(VI) anions by MS-HMS-PL. The isotherm curves for adsorption of Cr(VI) at 293 K are shown in Fig. 3e (figure caption for details) and corresponding isotherm parameters are tabulated in Table 4. For Cr(VI) adsorption on MS-HMS-PL, the Langmuir model provide the better approximation of R^2 ($R^2 = 0.9784$) than those of Freundlich ($R^2 = 0.8588$) and R-P models ($R^2 = 0.9752$). Moreover, the maximum adsorption capacity computed from the Langmuir model ($Q_{m,cal} = 270.14$ mg g^{-1}) was close to the maximum adsorption capacity achieved in this experiment ($Q_{m,exp} =$

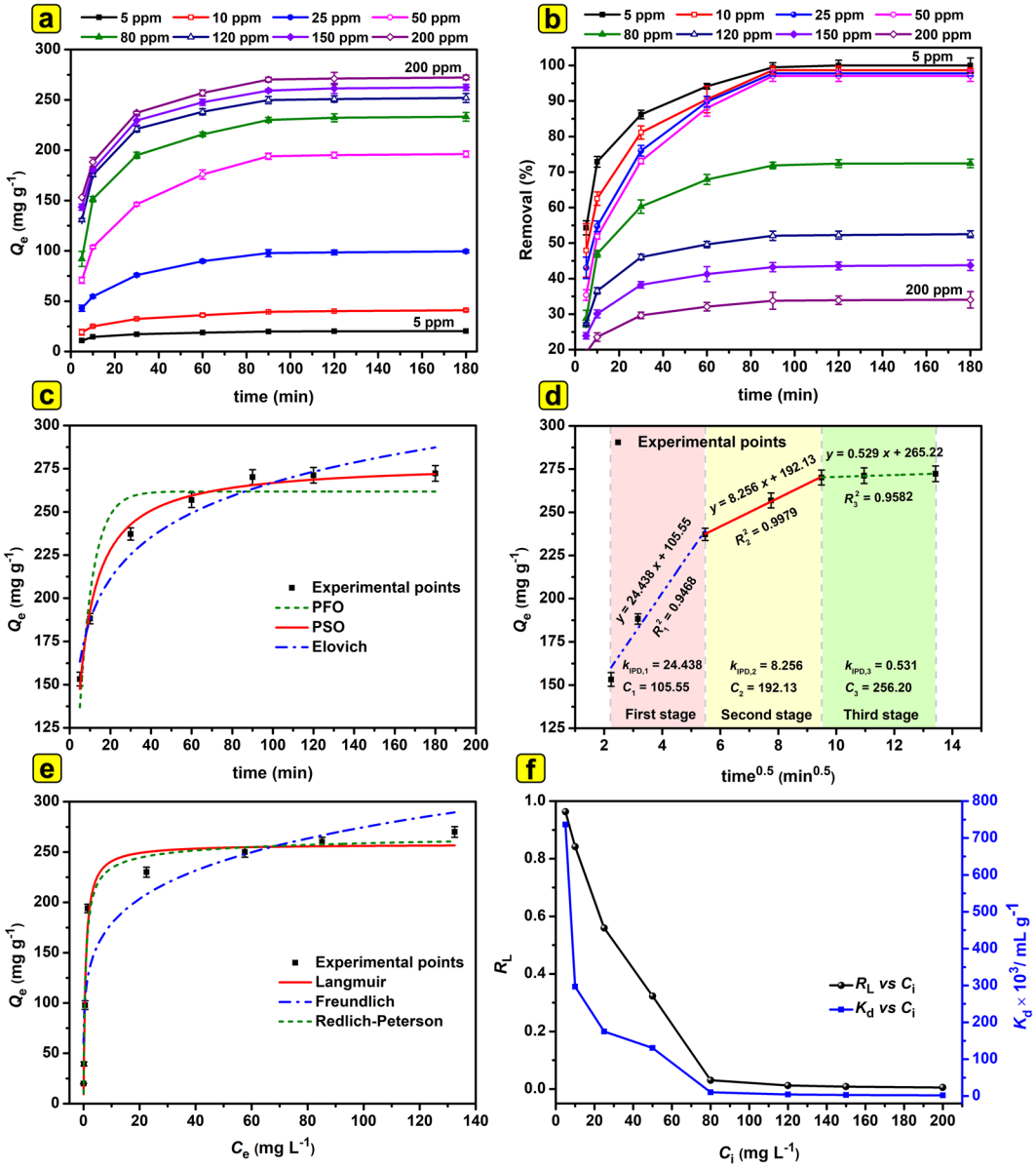

Figure 3. The effect of time and initial concentration on (**a**) adsorption capacity of adsorbent and (**b**) removal percentage of Cr(VI) under constant conditions (pH: 4.0; W: 5.0 mg; V: 20 ml; C_i: 5–200 mg L^{-1}; T: 293 K; shaking speed: 190 rpm; t: 5–180 min). (**c**) The experimental data and the nonlinear kinetics fitted to them and (**d**) the linear fitting of the IPD kinetic model (pH: 4.0; W: 5.0 mg; V: 20 ml; C_i: 200 mg L^{-1}; T: 293 K; t: 5–180 min). (**e**) The experimental data and the nonlinear isotherms fitted to them, and (**f**) the values of R_L and K_d *vs* C_i (pH: 4; W: 5.0 mg; V: 20 ml; C_i: 5–200 mg L^{-1}; T: 293 K; shaking speed: 190 rpm; t: 90 min).

257.67 mg g^{-1}) at 293 K, further demonstrating that the Langmuir isotherm model is better to express adsorption isotherm for Cr(VI) onto MS-HMS-PL.

Figure S5 discloses non-linear isotherm plots of Cr(VI) adsorption on the MS-HMS-PL at four different temperatures and their corresponding isotherm parameters are given in Table 4. The values of $Q_{m,cal}$ calculated for the Langmuir model for adsorption of Cr(VI) onto MS-HMS-PL were estimated to be 257.67 ($Q_{m,exp}$ =270.14 mg g^{-1}), 267.99 ($Q_{m,exp}$ = 282.89 mg g^{-1}), 275.55 ($Q_{e,exp}$ = 291.51 mg g^{-1}), and 281, 18 mg g^{-1} ($Q_{m,exp}$ = 302.02 mg g^{-1}) at 293, 303, 313, and 323 K, respectively.

A useful dimensionless parameter called separation factor (R_L, Table 2) is introduced in Langmuir's model to suggest the type of adsorption process where the values of $R_L = 0$, $R_L = 1$, $R_L > 1$, and $0 < R_L < 1$ imply that the adsorption process is irreversible, linear, unfavorable, and favorable, receptivity[8,24]. The values of R_L for adsorption of Cr(VI) onto MS-HMS-PL, as shown in Fig. 3f, lie between zero and unity, indicative of a favorable adsorption process.

Distribution coefficient values (K_d, mL g^{-1}, Eq. 4) could also be used to gain more insight into the favorability of the adsorption process under set conditions: $K_d \sim 10^2$ ($\sim$500 mL g^{-1}): acceptable; $K_d \sim 10^3$ ($\sim$5000 mL g^{-1}):

Model	Parameter	C_i (mg L^{-1}/ ppm)							
		5	10	25	50	80	120	150	200
PFO	$Q_{e,exp}$ (mg g^{-1})	19.89	39.47	97.77	194.05	230.15	249.82	259.30	270.14
	$Q_{e,cal}$ (mg g^{-1})	19.24	37.75	93.83	187.36	224.32	243.28	252.56	261.72
	k_1 (min^{-1})	0.1514	0.1168	0.090	0.0738	0.1038	0.1374	0.1430	0.1480
	R^2	0.9077	0.8906	0.8920	0.9310	0.9542	0.9384	0.9108	0.8905
PSO	$Q_{e,cal}$ (mg g^{-1})	20.48	40.86	103.01	208.45	244.78	260.01	269.27	278.55
	$k_2 \times 10^{-4}$ (g mg^{-1} min^{-1})	111.10	39.50	11.70	4.59	5.64	7.80	7.98	8.08
	h (mg g^{-1} min^{-1})	4.66	6.59	12.42	19.94	33.79	52.73	57.86	62.85
	R^2	0.9872	0.9830	0.9773	0.9875	0.9866	0.9978	0.9946	0.9893
Elovich	α (mg g^{-1} min^{-1})	58.62	37.51	48.08	60.14	142.18	498.95	635.99	782.76
	β (g mg^{-1})	0.3944	0.1676	0.0598	0.0272	0.0260	0.0294	0.0292	0.0290
	R^2	0.9301	0.9601	0.9652	0.9642	0.9159	0.9248	0.9418	0.9470
IPD	$k_{IPD,1}$ (mg g^{-1} $min^{-0.5}$)	1.810	3.93	9.975	22.334	29.308	26.306	25.512	24.438
	C_1 (mg g^{-1})	7.66	11.304	21.75	25.94	39.89	80.42	92.07	105.55
	R_1^2	0.7795	0.9405	0.9883	0.9431	0.7881	0.8909	0.9465	0.9468
	$k_{IPD,2}$ (mg g^{-1} $min^{-0.5}$)	0.665	1.744	5.466	11.985	8.778	7.173	7.448	8.256
	C_2 (mg g^{-1})	13.62	22.83	46.27	81.35	147.19	182.06	189.10	192.13
	R_2^2	0.9969	0.9967	0.9879	0.9917	0.9984	0.9981	0.9955	0.9979
	$k_{IPD,3}$ (mg g^{-1} $min^{-0.5}$)	0.106	0.412	0.417	0.540	0.746	0.530	0.772	0.529
	C_3 (mg g^{-1})	18.91	35.58	93.89	189.03	223.45	244.90	252.35	265.22
	R_3^2	0.9335	0.9986	0.9720	0.9636	0.9776	0.9582	0.7835	0.9582

Table 3. Kinetic parameter values after non-linear fitting (pH = 4.0, V = 20 mL, W = 5.0 mg, C_i = 5–200 mg L^{-1}, time = 5-180 min, T = 293 K, stirring rate = 190 rpm).

Model	Parameter	T (K)			
		293	303	313	323
Langmuir	$Q_{m,exp}$ (mg g^{-1})	270.14	282.89	291.51	302.02
	$Q_{m,cal}$ (mg^{-1})	257.67	267.99	275.55	281.18
	K_L (L mg^{-1})	1.412	1.572	1.751	1.853
	R^2	0.9784	0.9694	0.9780	0.9740
Freundlich	K_F ((mg g^{-1})(L mg^{-1})$^{1/n}$)	116.16	116.48	117.92	124.27
	n (−)	5.37	5.08	4.97	5.11
	R^2	0.8588	0.8430	0.8665	0.8632
R-P	K_{R-P}(L g^{-1})	401.36	407.92	434.07	579.82
	α_{R-P} (mg L^{-1}) $^{-g}$	1.691	1.651	1.794	2.397
	g (−)	0.9802	0.9803	0.9678	0.9625
	R^2	0.9752	0.9646	0.9771	0.9734

Table 4. Isotherm parameter values after non-linear fitting (pH = 4.0, V = 20 mL, W = 5.0 mg, C_i = 5-200 mg L^{-1}, time = 90 min, T = 293-323 K, stirring rate = 190 rpm).

very good; $K_d \geq 10^4$ (~50000 mL g^{-1}): outstanding[7,15,30,31]. In a removal process, the larger K_d values, the more affective the solid adsorbent is at holding and capturing the adsorbate. The K_d values for adsorption of Cr(VI) on MS-HMS-PL (Fig. 3f) were in the range of 2.04×10^3–7.37×10^5 mL g^{-1} in different initial Cr(VI) concentrations (5–200 mg L^{-1}). At initial concentrations of 5-50 mg L^{-1} K_d values ~10^5 were obtained. K_d values ~10^4 were obtained at initial concentration of 80 mg L^{-1}, and K_d values ~10^3 were attained between 120-200 mg L^{-1} initial concentration. Consequently, from the experimentally obtained values of K_d, MS-HMS-PL possesses outstanding (for C_i = 5–50 mg L^{-1}), very good (for C_i = 80 mg L^{-1}), and acceptable (for C_i = 120–200 mg L^{-1}) adsorption performance for removal of Cr(VI) from aqueous solution depending on the initial Cr(VI) concentration at constant conditions (pH: 4; W: 5.0 mg; V: 20 ml; C_i: 5–200 mg L^{-1}; T: 293 K; shaking speed: 190 rpm; t: 90 min).

Effect of temperature and thermodynamic studies. The influence of solution temperature on the adsorption capacity of adsorbent for Cr(VI) is shown in Fig. 4. The adsorption capacity increased as the solution temperature increased (Table 5, Fig. 4). To systematically characterize the physicochemical behavior of Cr(V) removal and to get a better insight into the mechanism of adsorption, the thermodynamic parameters of adsorption, *viz.*, $\Delta G^o_{ads.}$, $\Delta H^o_{ads.}$, and $\Delta S^o_{ads.}$, were estimated. These crucial parameters could be estimated from the temperature-dependent isotherms using the Eqs. (12–14) given in Table 1. Soltani *et al.*[5,8,24] and Lima *et al.*[32]

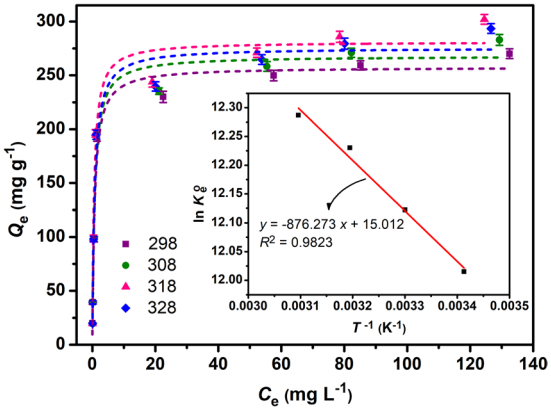

Figure 4. The effect of temperature on the adsorption capacity of MS-HMS-PL toward Cr(VI) from aqueous solution and its corresponding thermodynamic curve (inset) at 293, 303, 313, and 323 K under constant conditions (pH: 4.0; W: 5.0 mg; V: 20 ml; C_i: 200 mg L^{-1}; shaking speed: 190 rpm; t: 90 min).

$\Delta G^o_{ads.}$ kJ mol^{-1}					
293 K	**303 K**	**313 K**	**323 K**	$\Delta H^o_{ads.}$ kJ mol^{-1}	$\Delta S^o_{ads.}$ kJ mol^{-1} K^{-1}
−29.28	−30.53	−31.78	−33.03	+7.29	+0.13

Table 5. Thermodynamic parameters for adsorption of Cr(VI) on MS-HMS-PL (pH = 4.0, V = 20 mL, W = 5.0 mg, C_i = 5-200 mg L^{-1}, stirring rate = 190 rpm).

reported that the correct approach to calculating the aforementioned constants for an adsorption system is to perform non-linear fitting of the isotherms (usually Langmuir model) of the adsorption at various temperatures. For these calculations, it is considered that the aqueous solution of Cr(VI) is very diluted to consider that γ (the coefficient of activity, Eq. 12) is unitary. Thermodynamic equilibrium constants (K_e^o, Eq. 12) for each temperature could be calculated from the corresponding K_L values for each isotherm after fitting the Langmuir equation to the adsorption isotherms (Eq. 9). The values of ΔH^o_{ads} and ΔS^o_{ads} can be estimated from the slope and intercept of van't Hoff equation (the plot of In K_e^o versus $1/T$ in Eq. 13), respectively. The calculated thermodynamic parameters are given in Table 5. According to the literature, the $\Delta G^o_{ads.}$ (kJ mol^{-1}) and ΔH^o_{ads} (kJ mol^{-1}) values can explain the type of interaction using the following guideline: $\Delta H^o_{ads} > 60$, chemical bonding forces, $\Delta H^o_{ads} \approx 40$, exchange of dentate; $4 < \Delta H^o_{ads} < 10$, van der Waals interactions; $2 < \Delta H^o_{ads} < 40$, hydrogen bonding forces; $2 < \Delta H^o_{ads.} < 29$, dipole-dipole interactions; $-20 < \Delta G^o_{ads} < 0$, physisorption; $-400 < \Delta G^o_{ads} < -80$, chemisorption[10,24,33,34]. For the adsorption of Cr(VI), the ΔG^o_{ads} value ranged from $-33 < \Delta G^o_{ads} < -29$, indicating that the adsorption process of Cr(VI) on MS-HMS-PL was more of a spontaneous physisorption phenomenon rather than that of chemisorption. ΔH^o_{ads} (+7.29 kJ mol^{-1}) value, at the investigated temperatures, reveals that the adsorption process is the result of physical interactions such as electrostatic forces and van der Waals forces. Furthermore, the positive value of ΔH^o_{ads} clearly signifies that the interaction between the adsorbent and Cr(VI) anions is endothermic which was confirmed by the increase in adsorption capacity with increasing temperature. The positive value of ΔS^o_{ads} (+0.13 kJ mol^{-1} K^{-1}) means the randomness enhancement at the Cr(VI) solution/MS-HMS-PL interface in the adsorption process.

Comparative study. A comparison of the optimal conditions and adsorption performance of MS-HMS-PL for the adsorption of Cr(VI) with those of other adsorbent is shown in Table 6. It is clear that MS-HMS-PL showed high adsorption capacity for Cr(VI), calculated from Langmuir fitting, as compared to different synthetic, natural, and modified adsorbents. Such an outstanding removal capacity of MS-HMS-PL for Cr(VI) may be directly attributed to its high surface area and trimodal micro-meso-macroporous architecture which may provide fast mass transfer for adsorbate.

Conclusion

In this study, a hierarchical multi-shell hollow micro-meso-macroporous silica with pollen like morphology designated as MS-HMS-PL was synthesized *via* a facile soft-templating method. BET and TEM analyses revealed that MS-HMS-PL sub-microspheres possess a trimodal hierarchical pore structure including micropores (the major constituent of lamellar shells), mesopores (the minor constituent of lamellar shells), and macropores (in the middle of sub-microspheres). With its high surface area (414.5 m^2 g^{-1}), multi-shell structure, and facile synthesis route, MS-HMS-PL cloud be a good candidate for some applications such as adsorption, extraction, catalysis, and drug delivery. Accordingly, the adsorption performance of MS-HMS-PL for removal of Cr(VI) from aqueous solution was systematically studied. The effect of important adsorption factors—*viz*., pH. adsorbent dosage,

Adsorbent	$Q_{m,cal}$ (mg g^{-1})	pH	T (K)	*t* (min or h)	Ref.
bismuth hollow nanospheres	17.5	2.0	RT	—	[38]
Fe_3O_4/GO	32.33	4.5	293	5 h	[39]
EMCMCR	51.81	2.0	293	6–10 min	[40]
MSP	53.60	2.0	298	120 min	[41]
chitosan flakes	102	3.0	293	—	[42]
NMA-LDOs	103.4	—	303	150 min	[43]
magnetic poly(GMA–EGDMA) beads	140.6	2.0	298	120	[44]
G–MgAl-LDH nanocomposite	172.55	2.0	293	24 h	[45]
PANI@NC nanocomposites	198.04	1.0	298	480 min	[46]
MCS	200	natural	303	60	[47]
MHCSs	200	3.0	298	~700 min	[48]
MI-Cl-KCC-1	428	3.0–4.0	298	40 min	[5]
MS-HMS-PL	257.67	4.0	293	90 min	this study

Table 6. The comparison adsorption capacity of Cr(VI) under optimal conditions obtained by various adsorbents[a]. [a]Fe3O4/GO: porous Fe_3O_4 hollow microspheres/graphene oxide composite; EMCMCR: ethylenediamine-modified cross-linked magnetic chitosan resin; MSP: surfactant–modified serpentine; NMA-LDHs: Ni/Mg/Al layered double hydroxides; GMA–EGDMA: Glycidyl methacrylate-ethyleneglycol dimethacrylate; G–MgAl-LDOs: Graphene/MgAl-layered double oxides; PANI@NC: polyaniline grown on N-doped carbon nanoparticles; MCS: modified corn stalks; MHCSs: magnetic hollow carbon nanospheres; MI-Cl-KCC-1: N-methylimidazolium-functionalized KCC-1.

contact time, initial Cr(VI) concentration, and temperature—on the adsorption performance of MS-HMS-PL for Cr(VI) removal was evaluated. Kinetics, isotherms, and thermodynamic investigations were conducted to determine the adsorption mechanism and important parameters of adsorbent, and the non-linear fitting method was applied to calculated the kinetics and isotherms parameters. The estimated maximum adsorption capacity, according to the Langmuir model, was found to be 257.67 mg g^{-1} at pH 4.0, solution volume of 40 mL, the adsorbent dosage of 5.0 mg, the contact time of 90 min, stirring rate of 190 rpm, and solution temperature of 293 K.

Methods

Materials. Cetrimonium bromide (CTAB, ≥98.0%) and potassium dichromate ($K_2Cr_2O_7$, ≥99.5%) were purchased from Sigma-Aldrich (Buchs, Switzerland). 1-pentanol (≥98.5%), ammonium hydroxide ($NH_4^+OH^-$, 25% in water), silicon tetraethoxide (TEOS, ≥99.0%), sodium hydroxide pellets (NaOH, 99%), and fuming hydrochloric acid (HCl, 37%) were purchased from Merck (Darmstadt, Germany). Ethanol (96.0%) was prepared from Bidestan Co. (Ghazvin, Iran). Deionized (DI) water was utilized for the adsorption investigations and preparation of the adsorbent.

Synthesis of MS-HMS-PL. In a typical synthesis route, in a 250 mL bottle made from high-density polypropylene (HDPP) with a leakproof screw cap, 1.800 g CTAB was dissolved in 90 mL of pure water with magnetically stirring at 293 K for 10 min. Then, 7.7 mL of $NH_4^+OH^-$ was added to the bottle and the mixture was stirred for 20 min. Afterward, 2.7 mL of 1-pentanol was added to the mixture and stirred for 15 min followed by adding 7.5 mL of TEOS. The mixture was stirred at 293 K for 2 h and then maintained at an electric oven (343 K) for 24 h. The obtained white gel was washed with pure water and ethanol (96%) and dried at 333 K for 24 h. Finally, the white powder was calcined at 823 K for 6 h so as to remove the organic template CTAB.

Batch experiments. Batch adsorption studies were conducted in 50-mL HDPP bottles with a leakproof screw cap and a constant working volume of 20 mL in an incubator-shaker apparatus at a shaking speed of 190 rpm. 1000 mg L^{-1} stock solution of Cr(VI) was prepared by mixing the appropriate mass of $K_2Cr_2O_7$ in pure water. Working standard solutions with desired Cr(VI) concentrations (5-200 mg L^{-1}) were prepared by suitable dilutions of Cr(VI) stock solution just before use. For each experiment, a certain amount of adsorbent (2.0, 5.0, 8.0, and 15.0 mg) was transferred to a 50-mL HDPP bottle containing 20 mL of Cr(VI) solutions with desired pH (2.0–8.0) and Cr(VI) concentration (5–200 mg L^{-1}), and then agitated at 190 rpm at a certain temperature (293, 303, 313, and 323 K). The pH of the solutions was adjusted with 0.1 mg L^{-1} NaOH and HCL solutions. After specific time intervals (5–200 min), the Cr(VI)-loaded adsorbent particles were separated by centrifugation (3500 rpm, 5 min). The adsorption capacities of adsorbent at any time *t* (Q_t, mg g^{-1}), the adsorption capacity at equilibrium (Q_e, mg g^{-1}), and removal percentage were determined according to the following formula:

$$Q_t = (C_i - C_t) \cdot V/W \quad (1)$$

$$Q_e = (C_i - C_e) \cdot V/W \quad (2)$$

$$\%\ \text{Removal} = 100 \cdot (C_i - C_e)/C_i \quad (3)$$

where C_i is the initial adsorbate concentration (mg L^{-1}), C_t is the adsorbate concentration at a certain time t (mg L^{-1}), C_e is the adsorbate concentration at equilibrium (mg L^{-1}), V is the volume of the liquid phase (L), and W is the mass of the adsorbent (mg).

The values of distribution coefficient (K_d, mL g^{-1}) at equilibrium can be calculated from the following formula:

$$K_d = \frac{(C_i - C_e) \cdot V}{C_i \cdot W} = \frac{Q_e}{C_e} \quad (4)$$

Characterization. Low angle X-ray diffraction (L-XRD) analysis, Fourier transform infrared (FT-IR) spectroscopy, nitrogen adsorption-desorption measurement at 77 K, field emission scanning electron microscopy (FE-SEM), and transmission electron microscopy (TEM), were used for the characterization of the sample. Also, flame atomic absorption spectroscopy (FAAS) was used for the determination of the Cr(VI) concentration in the aqueous solutions. The details of the apparatus used in this work are given in Supplementary Information (S1. Experimental section, Apparatus).

Received: 25 March 2020; Accepted: 22 May 2020;
Published online: 17 June 2020

References

1. Zhang, S. *et al*. Formation of Fe_3O_4@MnO_2 ball-in-ball hollow spheres as a high performance catalyst with enhanced catalytic performances. *J. Mater. Chem. A* **4**, 1414–1422 (2016).
2. Wang, X., Feng, J., Bai, Y., Zhang, Q. & Yin, Y. Synthesis, properties, and applications of hollow micro-/nanostructures. *Chem. Rev.* **116**, 10983–11060 (2016).
3. Wang, J. *et al*. pH-regulated synthesis of multi-shelled manganese oxide hollow microspheres as supercapacitor electrodes using carbonaceous microspheres as templates. *Adv. Sci* **1**, 1400011 (2014).
4. Qi, J. *et al*. Multi-shelled hollow micro-/nanostructures. *Chem. Soc. Rev.* **44**, 6749–6773 (2015).
5. Soltani, R., Marjani, A., Hosseini, M. & Shirazian, S. Synthesis and characterization of novel N-methylimidazolium-functionalized KCC-1: A highly efficient anion exchanger of hexavalent chromium. *Chemosphere* **239**, 124735 (2020).
6. Soltani, R., Marjani, A. & Shirazian, S. Facile one-pot synthesis of thiol-functionalized mesoporous silica submicrospheres for Tl(I) adsorption: isotherm, kinetic and thermodynamic studies. *J. Hazard. Mater.* **371**, 146–155 (2019).
7. Soltani, R., Shahvar, A., Gordan, H., Dinari, M. & Saraji, M. Covalent triazine framework-decorated phenyl-functionalised SBA-15: its synthesis and application as a novel nanoporous adsorbent. *New J. Chem.* **43**, 13058–13067 (2019).
8. Zarei, F., Marjani, A. & Soltani, R. Novel and green nanocomposite-based adsorbents from functionalised mesoporous KCC-1 and chitosan-oleic acid for adsorption of Pb (II). *Eur. Polym. J.* **119**, 400–409 (2019).
9. Soltani, R., Marjani, A., Hosseini, M. & Shirazian, S. Mesostructured Hollow Siliceous Spheres for Adsorption of Dyes. *Chem. Eng. Technol.* **43**, 392–402 (2020).
10. Soltani, R., Marjani, A., Hosseini, M. & Shirazian, S. Meso-architectured siliceous hollow quasi-capsule. *J. Colloid Interface Sci.* **570**, 390–401 (2020).
11. Ren, H. & Yu, R. Hollow multi-shelled structures for energy conversion and storage applications. *Inorg. Chem. Front* **6**, 2239–2259 (2019).
12. Gu, D. *et al*. An aqueous emulsion route to synthesize mesoporous carbon vesicles and their nanocomposites. *Adv. Mater.* **22**, 833–837 (2010).
13. Huang, C.-C., Huang, W. & Yeh, C.-S. Shell-by-shell synthesis of multi-shelled mesoporous silica nanospheres for optical imaging and drug delivery. *Biomaterials* **32**, 556–564 (2011).
14. Ma, X. *et al*. Tunable construction of multi-shell hollow SiO_2 microspheres with hierarchically porous structure as high-performance anodes for lithium-ion batteries. *Chem. Eng. J* **323**, 252–259 (2017).
15. Soltani, R., Marjani, A. & Shirazian, S. Shell-in-shell monodispersed triamine-functionalized SiO_2 hollow microspheres with micro-mesostructured shells for highly efficient removal of heavy metals from aqueous solutions. *J. Environ. Chem. Eng.* **7**, 102832 (2019).
16. Zheng, Y., Cheng, B., You, W., Yu, J. & Ho, W. 3D hierarchical graphene oxide-NiFe LDH composite with enhanced adsorption affinity to Congo red, methyl orange and Cr(VI) ions. *J. Hazard. Mater.* **369**, 214–225 (2019).
17. Zhang, B., Hu, R., Sun, D., Wu, T. & Li, Y. Fabrication of chitosan/magnetite-graphene oxide composites as a novel bioadsorbent for adsorption and detoxification of Cr(VI) from aqueous solution. *Sci. Rep* **8**, 1–12 (2018).
18. Kulkarni, P. S. *et al*. Valorization of Uncharred Dry Leaves of Ficus benjamina towards Cr(VI) removal from Water: Efficacy Influencing Factors and mechanism. *Sci. Rep.* **9**, 1–12 (2019).
19. Soltani, R., Dinari, M. & Mohammadnezhad, G. Ultrasonic-assisted synthesis of novel nanocomposite of poly (vinyl alcohol) and amino-modified MCM-41: a green adsorbent for Cd(II) removal. *Ultrason. Sonochem* **40**, 533–542 (2018).
20. Soltani, R., Marjani, A., Moguei, M. R. S., Rostami, B. & Shirazian, S. Novel diamino-functionalized fibrous silica submicro-spheres with a bimodal-micro-mesoporous network: ultrasonic-assisted fabrication, characterization, and their application for superior uptake of Congo red. *J. Mol. Liq.* **294**, 111617 (2019).
21. Innocenzi, P., Falcaro, P., Grosso, D. & Babonneau, F. Order− disorder transitions and evolution of silica structure in self-assembled mesostructured silica films studied through FTIR spectroscopy. *J. Phys. Chem. B* **107**, 4711–4717 (2003).
22. Thommes, M. *et al*. Physisorption of gases, with special reference to the evaluation of surface area and pore size distribution (IUPAC Technical Report). *Pure Appl. Chem* **87**, 1051–1069 (2015).
23. Liu, J. *et al*. A facile vesicle template route to multi-shelled mesoporous silica hollow nanospheres. *J. Mater. Chem.* **20**, 4595–4601 (2010).
24. Soltani, R., Marjani, A. & Shirazian, S. A hierarchical LDH/MOF nanocomposite: single, simultaneous and consecutive adsorption of a reactive dye and Cr(vi). *Dalton Trans.* **49**, 5323–5335 (2020).
25. Guo, L., Li, G., Liu, J., Meng, Y. & Xing, G. Nonlinear analysis of the kinetics and equilibrium for adsorptive removal of Cd(II) by starch phosphate. *J. Dispersion Sci. Technol* **33**, 403–409 (2012).
26. Kumar, K. V. & Sivanesan, S. Selection of optimum sorption kinetics: comparison of linear and non-linear method. *J. Hazard. Mater.* **134**, 277–279 (2006).
27. Foo, K. Y. & Hameed, B. H. Insights into the modeling of adsorption isotherm systems. *Chem. Eng. J* **156**, 2–10 (2010).
28. Kosmulski, M. Isoelectric points and points of zero charge of metal (hydr) oxides: 50 years after Parks' review. *Adv. Colloid Interface Sci.* **238**, 1–61 (2016).
29. Hegyesi, N., Vad, R. T. & Pukánszky, B. Determination of the specific surface area of layered silicates by methylene blue adsorption: The role of structure, pH and layer charge. *Appl. Clay Sci.* **146**, 50–55 (2017).

30. Yantasee, W. *et al*. Removal of heavy metals from aqueous systems with thiol functionalized superparamagnetic nanoparticles. *Environ. Sci. Technol.* **41**, 5114–5119 (2007).
31. Fryxell, G. E. *et al*. Actinide sequestration using self-assembled monolayers on mesoporous supports. *Environ. Sci. Technol.* **39**, 1324–1331 (2005).
32. Lima, E. C., Hosseini-Bandegharaei, A., Moreno-Piraján, J. C. & Anastopoulos, I. A critical review of the estimation of the thermodynamic parameters on adsorption equilibria. Wrong use of equilibrium constant in the Van't Hoof equation for calculation of thermodynamic parameters of adsorption. *J. Mol. Liq.* **273**, 425–434 (2019).
33. Zhou, Y. *et al*. Removal of crystal violet by a novel cellulose-based adsorbent: comparison with native cellulose. *Ind. Eng. Chem. Res.* **53**, 5498–5506 (2014).
34. Qiu, T., Zeng, Y., Ye, C. & Tian, H. Adsorption thermodynamics and kinetics of p-xylene on activated carbon. *J. Chem. Eng. Data* **57**, 1551–1556 (2012).
35. Dong, Z. *et al*. Quintuple-shelled SnO_2 hollow microspheres with superior light scattering for high-performance dye-sensitized solar cells. *Adv. Mater.* **26**, 905–909 (2014).
36. Hwang, S. H., Yun, J. & Jang, J. Multi-Shell Porous TiO_2 Hollow Nanoparticles for Enhanced Light Harvesting in Dye-sensitized Solar Cells. *Adv. Funct. Mater.* **24**, 7619–7626 (2014).
37. Park, G. D., Lee, J.-H., Lee, J.-K. & Kang, Y. C. Effect of esterification reaction of citric acid and ethylene glycol on the formation of multi-shelled cobalt oxide powders with superior electrochemical properties. *Nano Res* **7**, 1738–1748 (2014).
38. Qin, F. *et al*. Large-scale synthesis of bismuth hollow nanospheres for highly efficient Cr (VI) removal. *Dalton Trans.* **41**, 11263–11266 (2012).
39. Liu, M. *et al*. Synthesis of porous Fe_3O_4 hollow microspheres/graphene oxide composite for Cr(VI) removal. *Dalton Trans.* **42**, 14710–14717 (2013).
40. Hu, X.-j *et al*. Adsorption of chromium (VI) by ethylenediamine-modified cross-linked magnetic chitosan resin: isotherms, kinetics and thermodynamics. *J. Hazard. Mater.* **185**, 306–314 (2011).
41. Mobarak, M. *et al*. Surfactant–modified serpentine for fluoride and Cr(VI) adsorption in single and binary systems: Experimental studies and theoretical modeling. *Chem. Eng. J* **369**, 333–343 (2019).
42. Aydın, Y. A. & Aksoy, N. D. Adsorption of chromium on chitosan: Optimization, kinetics and thermodynamics. *Chemical Engineering Journal* **151**, 188–194 (2009).
43. Lei, C. *et al*. Superb adsorption capacity of hierarchical calcined Ni/Mg/Al layered double hydroxides for Congo red and Cr(VI) ions. *J. Hazard. Mater.* **321**, 801–811 (2017).
44. Bayramoğlu, G. & Arica, M. Y. Adsorption of Cr(VI) onto PEI immobilized acrylate-based magnetic beads: isotherms, kinetics and thermodynamics study. *Chem. Eng. J* **139**, 20–28 (2008).
45. Yuan, X. *et al*. Calcined graphene/MgAl-layered double hydroxides for enhanced Cr(VI) removal. *Chem. Eng. J* **221**, 204–213 (2013).
46. Lai, Y. *et al*. UiO-66 derived N-doped carbon nanoparticles coated by PANI for simultaneous adsorption and reduction of hexavalent chromium from waste water. *Chem. Eng. J* **378**, 122069 (2019).
47. Chen, S., Yue, Q., Gao, B., Li, Q. & Xu, X. Removal of Cr(VI) from aqueous solution using modified corn stalks: Characteristic. *equilibrium, kinetic and thermodynamic study. Chem. Eng. J* **168**, 909–917 (2011).
48. Zhang, L.-H., Sun, Q., Liu, D.-H. & Lu, A.-H. Magnetic hollow carbon nanospheres for removal of chromium ions. *J. Mater. Chem. A* **1**, 9477–9483 (2013).

Author contributions

Roozbeh Soltani conceived the idea of preparing MS-HMS-PL material, designed the study on the synthesis of MS-HMS-PL material, synthesized and characterized MS-HMS-PL, conducted the adsorption studies, computed the theoretical adsorption data, analyzed the results, supervised the project, and wrote and edited the paper. Azam Marjani gathered experimental adsorption data by flame atomic absorption spectroscopy, contributed to the final manuscript, and also provided chemicals and laboratory equipment. Reza Soltani gathered experimental adsorption data by flame atomic absorption spectroscopy. Saeed Shirazian supervised the findings of this work, supervised the project, provided chemicals and laboratory equipment, and edited the paper. All authors verified the analytical methods.

Competing interests

The authors declare no competing interests.

Additional information

Supplementary information is available for this paper at https://doi.org/10.1038/s41598-020-66540-6.

Correspondence and requests for materials should be addressed to S.S.

Reprints and permissions information is available at www.nature.com/reprints.

Publisher's note Springer Nature remains neutral with regard to jurisdictional claims in published maps and institutional affiliations.